TiFM2.0 - Versatile mechanical measurement and actuation in live embryos

Ana R. Hernandez-Rodriguez[1,2,4], Yisha Lan[1,2,4], Fengtong Ji[1,2], Susannah B.P. McLaren[1,2], Joana M. N. Vidigueira[1,2], Ruoheng Li[1], Yixin Dai[1,3], Emily Holmes[1,2], Lauren D. Moon[1,2], Lakshmi Balasubramaniam[1,2], Fengzhu Xiong[1,2,*]

[1]Wellcome Trust / CRUK Gurdon Institute, University of Cambridge, Cambridge, United Kingdom
[2]Department of Physiology, Development and Neuroscience, University of Cambridge, Cambridge, United Kingdom
[3]Life Science Institute, Zhejiang University, Hangzhou, China
[4]These authors contributed equally to this work.
*fx220@cam.ac.uk

SUMMARY

During development, spatial-temporally patterned tissue-level stresses and mechanical properties create diverse tissue shapes. To understand the mechanics of small-scale embryonic tissues, precisely controlled sensors and actuators are needed. Previously, we reported a control-based approach named tissue force microscopy (TiFM1.0), which combines dynamic positioning and imaging of an inserted cantilever probe to directly measure and impose forces in early avian embryos. Here we present an upgraded system (TiFM2.0) that utilises interferometer positioning to minimise probe holder footprint, enhancing accessibility and imaging signal. This new design enables a double-probe configuration for bidirectional stretching, compression and stress propagation experiments. As proof-of-concept, we showcase a variety of examples of TiFM2.0 applications in chicken and zebrafish embryos, including the characterization of mechanical heterogeneities important for the morphogenesis of the chicken posterior body axis. We also present simplified designs and protocols for the replication of TiFM systems with minimal custom engineering for developmental biology labs.

INTRODUCTION

Multicellular organisms create tissue shapes throughout development by actively regulating mechanical forces and tissue material properties through patterned cell activities[1–6]. These mechanical factors also provide feedback to cell behaviours and genetic regulation, forming a close interplay that contributes to the robustness of morphogenesis[7–11]. Such interplays are deeply embedded in the evolution history of development and work across scales, leading to a high degree of complexity. Disentangling these complexities would require quantitative measurement and control of tissue mechanics, integrated with molecular and cellular approaches, such as -omics[12] and high-resolution live imaging[13]. These precision mechanical tools are also expected to impact engineering efforts that aim to recreate tissue and organs of functional shapes[14].

Existing *in vivo* tissue mechanics approaches can be categorised largely by the presence or absence of direct contact with the sample. Non-contact methods include light and acoustic imaging of the sample and interpretation of the returned signal

under certain assumptions, such as tissue geometry, composition and viscoelastic behaviours. The signals range from the expression and dynamics of key cytoskeleton-related molecules[15,16], their associated sensors[17], cell shapes and movements[18,19], cell/tissue recoils triggered by laser ablation[20] or optogenetics[21,22], to scattering patterns and spectrum shifts[23–25]. These approaches offer accessibility with low-invasiveness and can cover large tissue areas. The disadvantages are that they often do not yield quantitatively definitive results as the measurements usually capture only a fraction of the factors that contribute to the tissue forces and properties, and assumptions used in data interpretation can strongly bias the conclusions. For example, inferring junctional tension and pressure from image analysis often assumes equilibrium conditions and does not consider the 3D nature of biological tissues[26]. On the other hand, contact methods utilise an inserted or injected sensor, usually with known and/or controllable mechanical properties, to directly detect its interactions with cells and tissues. The signals recorded can be directly imaged deformations and deflections[27–32], sometimes also measured through other means such as electrical currents[33]. Whilst providing definitive measurements enabling the establishment of the regimes of forces and mechanical properties in which developing tissues operate, the results from these approaches must be interpreted carefully, considering the effective spatial-temporal resolution and scales. In particular, whether the scales are relevant to tissue morphogenesis and how the invasiveness of sensors to the local tissue environment causes mechanical artefacts. Furthermore, considerable probe design and precision engineering expertise[27,29,34–36] is often required in developing and deploying mechanical sensors for small and soft embryonic tissues, reducing the throughput and applicability of such systems for wide use in the developmental biology community.

The prototype TiFM system (TiFM1.0)[29] is a cantilever-based measurement and actuation tool that vertically inserts a soft atomic force microscope (AFM) probe into intact, live embryonic tissues. The probe deflects under the morphogenetic forces from the tissue or imposed forces by the motorized holder. Real-time, precise measurements of the positions of the probe tip and holder allow the force to be quantified and controlled dynamically. TiFM1.0 used charged capacitors to monitor the position of the cantilever holder, which results in a large probe head that limits sample illumination. The capacitors are also sensitive to the humidity in the environment of the embryo sample, where condensations could cause discharges that affect the measurements. Another challenge associated with limited access space on top of the sample is that further modifications, such as multiplexing of the probes, are not allowed. Here we overcome these challenges by incorporating interferometer-based positioning, greatly reducing the probe head footprint. This new design allows for improved top illumination, a stage mounted incubation chamber and a double-arm probe holder to be added. These modifications expand the applications possible to include different types of stress loading and rheological measurements, and enhanced coverage and reliability to provide a new generation of tissue force microscopy (TiFM2.0), suitable for studying a variety of tissue mechanics questions in live embryos.

RESULTS

Design and operation of the TiFM2.0 system. TiFM2.0 (Figure 1A) utilizes a probe head containing 2 electrical piezos in parallel, enabling independent and fine

positioning of two probes along the X axis through a voltage controller. The whole probe head is adjustable by a 3-axis micromanipulator, while the left piezo has a separate 2-axis (YZ) micromanipulator for fine alignment of 2 probes relative to each other. The overall much smaller probe head construct (compared to TiFM1.0[29]) can be lowered into an environmental well fitted with a controlled heating holder and a water supply micropipette, where standard glass-bottom sample dishes fit. To maximize the flexibility and range of interactions between the 2 probes, we designed the holder for AFM chips on an inclined surface (Figure 1B). The inner surface (between two holders) has an angle of 11.3° to the vertical plane and the outer surface has a 20° inclination to the vertical plane. This allows the distance between two AFM chips to vary between a few hundred µm on the negative (*i.e.*, the two probes crossing each other) to >1 mm which provides wide operating space for different tissue sizes and functions including stretching, compressing and twisting. The mounting surface of the holder supports a mirror for the interferometer lasers to measure probe holder positions from the sides. The probes and sample are imaged from the bottom side via a wide-field fluorescent microscope with a high framerate camera (Figures 1C-D). Note that given the system design, the probe holder configuration is modular so that a single probe can also be used, depending on the experiment. The micromanipulators can be further automated for programmable probe alignments, and the microscope can be changed to a high-resolution inverted confocal microscope or a fast oblique plane light-sheet microscope (OPM)[37,38] depending on the applications required.

An experiment on TiFM2 follows a set-up sequence where probes are aligned with samples in 3D coordinates and a control run is performed where probe movement together with the holder without resistance is recorded by the microscope and the interferometer (Figure 1E); then a measurement sequence where samples are inserted and actuated with the probe(s) under the control of a user-defined program (Figure 1F). To begin, the sample is first mounted on the microscope stage to determine the desired focal plane of imaging (e.g., the tissue of interest) and also the sample surface along the z-axis (z, z_0). These are recorded by the z-focus or stage controller of the base microscope; next, the sample is removed and the probes are lowered with the micromanipulators to align with the imaging plane to perform a control sequence. This data contains synchronized live imaging along with the interferometer signal, allowing the establishment of the one-to-one relationship ($x_T=f(x_C)$, mostly linear within the operational range) between the holder location (x_C) and the probe's tip x location (x_T, obtained from tracking) (Figure 1E). Samples are then returned to the microscope stage, and the probes are inserted carefully until the tips are in sharp focus at the desired z depth (z). The measurement or actuation is then performed to produce position data tracks of the holder (x_{C1}) and the probe inside the sample (x_{T1}) (Figure 1F). The stress on the probe along the x axis at any time point is then given a by $\sigma = k\cos(\theta)[f(x_{C1})-x_{T1}]w^{-1}(z-z_0)^{-1}$, where k is the spring constant, w is the width of the probes and θ is the insertion angle relative to the z axis. The strain field of the samples can be measured by tracking markers and features from the images. Combining these data, sample stresses and responses could be determined, and used to assess its mechanical properties quantitatively with finite element models[39] if needed.

Local stretching and compression of small embryonic tissues. A key technical challenge in mechanically perturbing early embryonic tissue is to apply controlled,

physiologically relevant forces and deformations. With TiFM systems we are now able to apply small forces in a minimally invasive manner in the intact embryo[29]. In the example of the pre-somitic mesoderm (PSM), we performed local stretching with TiFM2.0 to compare the tissue responses in the anterior versus posterior PSM (*i.e.* aPSM vs. pPSM), regions known to have a transition of cell state[40,41] (mesenchymal posterior to epithelial anterior), cell density[9,42] (low posterior to high anterior) and extracellular matrix (ECM) enrichment[43,44] and distribution[45]. A course of stepwise stretching along the anterior-posterior axis, followed by probe holding and relaxation by probe retrieval was performed in the mediolateral centres of the aPSM and pPSM (Figure 2A). The tissues showed distinct responses and dynamics towards a similar final holding strain. In the aPSM, micro-tearing (Figure 2A', arrows) appeared on the tissue to the inside of the probe tips, indicating tension build-up around the edges of the probes during stretching. In contrast, in the pPSM no tearing appeared (Figure 2A''). At both locations, an increase of neural tube wall curvature towards the PSM under stretching was observed, indicating close links between the tissues that allow transmission of forces from the transverse contraction of the PSM under stretching to the neural tube. These tissue behaviours are unchanged by the presence of the endoderm which the probes go through from the ventral side to reach the PSM. We measured the strain dynamics of the tissue between the probes effectively as the distance increase between the 2 probes over the initial distance (Figure 2B). After each step movement of the motors, the probes in the pPSM were found to stabilize positions more quickly compared to the probes in the aPSM, which showed a more gradual creep. This difference is particularly apparent at higher strains (Figure 2B, arrows). Upon probe retrieval after 5 minutes of holding, the tissues (now tracked manually by the insertion wound sites) both retracted, with the aPSM shortening faster and to a larger extent over time (Figure 2C). These results show that the aPSM is stiffer and more viscous than the pPSM in their native locations *in vivo*. Additionally, the deformation of tissues under the imposed forces can be analysed in terms of cell shape and arrangement changes (Figures 2A'-A''). Cells can be observed to elongate along the expected tension patterns (e.g., extensive between the probes and compressive on the outer sides of the probes). To further test the potential of using the mechanical probes to alter cell shapes, we used Tg(CAG:memGFP)[46] embryos and stretched the epiblast of HH4 embryos (Figure 2D, Movie S1). Cell shapes can be seen to change and distances between cells increase along the direction of imposed tension. These results demonstrate TiFM2.0's capacity to deliver local cell shape and mechanical perturbations in developing tissues.

To test the ability of TiFM2.0 to modulate key morphogenetic events, we sought to promote or undo the folding process of the epithelial neural tube. During neurulation, the neural plate bends dorsally towards closure at the midline to form the tube, driven by a combination of tissue-intrinsic and -extrinsic forces[1], such as apical constriction[47], apoptosis[48], ectoderm tension[49,50] and PSM compression[9]. The probes are first calibrated through synchronised control in both compressive and expansive directions (Figures 3A-B). After anchoring the probes on both sides of the neural fold edge, a sequence was performed to push the neural folds closer together and then to split them (Figure 3C), using the same conditions as the control sequence (Figure 3B). Comparing the probe positions in the tissue with the expected no-resistance positions from the calibration curve yields the forces at different folding states (Figures 3C-D). The measured forces on the probes are at the 1-10μN scale

between overly apposed to widely open neural folds, providing information of the resistance to deformation of the neural plate tissue in its native environment. For example, these forces are 1-2 order of magnitude higher than recently measured native forces that drive folding, such as the compressive force from the pPSM (~100nN) measured by TiFM1.0[29] and the net compressive forces inside the anterior neural folds (~100nN) measured by an iMeSH cylinder[51], which drive comparatively much slower tissue deformation (order of 1hr as compared to ~10s here) during normal morphogenesis of the neural tube.

Using compression of the posterior body axis and following its subsequent relaxation, we can analyse the heterogeneity of tissue mechanical properties spatially[11]. When the compression comes from the posterior-to-anterior direction, we observed higher levels of compression occurring close to the probe, whilst tissues further anterior show a decreased/minimal amount of deformation (Figure 4A). Upon probe retraction after 5min holding, the posterior tissues retain a significant amount of deformation. In contrast, when the compression comes from the lateral-to-medial axis, tissue deformation propagates further to the contralateral side, and the recoil is much stronger after probe retraction (Figure 4B). These results show that the developing body axis is deformable along the anterior-posterior axis while resistant along the medial-lateral axis. This pattern favours tissue elongation in a bilaterally symmetric manner. To test this in a developmentally relevant timescale, we performed the lateral-medial bending on a cultured embryo using a notochord-anchored probe and held the deformation for 1 hour (Figure 4C). Unlike the 1-minute control that elastically restored the initial tissue shape, the 1-hour embryo exhibited a slow creep during holding and showed 10-30μm of residual deformation after probe retraction. This is far less than the extra elongation along the anterior-posterior axis achievable by a 1-hour pulling[29] (~150 μm) under a similar force. These data show that while increased plastic deformation is observed following persistent stress, the different deformability of the body axis between the anterior-posterior and medial-lateral directions is consistent between short and long timescales.

Dynamic mechanical measurements. TiFM2.0 enables a variety of mechanical measurements. For tissue forces, in addition to previously reported single-direction stalling stress measurement[29], the 2nd parallel probe allows pinning and clamping of tissues that are not normally held down by other structures. In the example of the early blood vessels, which lay elevated on the ventral side of the embryo above the yolk sac, the probes can be used to clamp the vessel in place and measure blood pressure (Figures 5A-D). The heartbeats are unaffected by the presence or engagement of the probes (Figure 5E). The rhythmic change of blood pressure is absorbed by the expansion of the vessel and is not detectable while the probes are not clamping onto the vessel (Figure 5C,F). During clamping, the probe tip can be observed to move with the vessel wall. The peak-valley difference varies between 5-10μm, which provides an estimate of pressure differential at ~20Pa (probe force constant k = 0.03N/m, and the contact area at the order of $10^{-8}m^2$).

TiFM2.0 also enables *in situ* probing of tissue mechanical properties, taking advantage of accurate dynamic positioning and sensitive soft probes. To test this capacity, we inserted a single probe into water and a semidilute polymer solution of 8.5% poly-isobutylene in hexadecane (PIB), a reference viscoelastic fluid (SRM 2490). The probe was then driven to oscillate using a sine function with a given

maximum voltage and frequency while the tip was tracked (Figures 6A-B). After the resultant tracks were fitted to a sinusoidal function, the interferometer signals were aligned on the time axis to contrast the difference of probe movement between PIB and water (Figure 6B, i). As expected, the probe shows a smaller amplitude and more phase shift in PIB, indicating viscoelastic resistance to probe movement. Across different motor ranges, frequencies and insertion depths the probes overall show a smaller magnitude of oscillation in PIB (Figure 6C). At lower frequencies, the probe shows more difference in magnitude between water and PIB, and the sensitivity is higher for shallow insertions (Figure 6C). To test this in tissue-like solids, we compared the amplitude of oscillation between PBS and a series of hydrogels of increasing stiffness at two different depths that are representative of experimental conditions in embryos (Figures 6B, ii, 6D, Movie S2). Overall, we observed lower amplitudes as stiffness increased in a quantitative relationship that would allow differences in amplitude to be related back to differences in the material properties of the samples. Probes with lower force constants (e.g. k = 0.03N/m) can be used for samples at the softer ranges. Of note, at deeper insertions in stiffer gels, the oscillation of the probe tip is antiphase to the imposed sinewave motor motion and is represented as negative, due to the strong resistance bending the probe at a higher z-axis point. We next interrogated chicken embryo body axis tissues utilising this method, following the conditions of Figure 6D. The notochord shows a strong restriction on probe movement, whereas PSM is much less resistant (Figures 6E-F, Movie S3). In the dorsal neural tube, the hindbrain shows less resistance to probe movement compared with the spinal cord (Figure 6G). These results are consistent with previous studies assessing the deformability of these tissues using other methods[30,52]. However, it should be noted that keeping track of the spatial range of tissue deformation by the probe is important for the interpretation of these results. For solid tissues, the resistance to probe movement measured could indicate the neighbouring tissue connections and boundaries rather than local properties around the probe, which can be much stronger. A solution to this challenge is to use the second probe on TiFM2.0 to provide a defined spatial range and act as a receiving end of the mechanical signal. We tested this in the PSM where small mechanical differences between the anterior and posterior exist, as shown by stretching experiments (Figures 2B-C). Indeed, the mechanical wave propagates with a smaller magnitude loss in the aPSM as compared to the pPSM, indicating that aPSM is more solid-like while pPSM is more liquid-like relatively (Figures 6H-I). These results are consistent with the reported cell and ECM organisation of the PSM along the AP axis[44,45], and the droplet-based rheological measurements in the zebrafish PSM[53], showing conservation of the PSM mechanical property gradient among vertebrates despite distinct tissue sizes and ECM organisations. Together, our results demonstrate TiFM2.0's capacity for direct *in vivo*, *in situ* tissue mechanical property assessment.

To expand the capacity of TiFM2.0 beyond the thin, flat avian early embryo tissues, we extended the back end of the probe with a DiI bead (Figure 7A) which provides high-contrast fluorescent signal and additional spatial coverage when the probe front becomes obscured by thicker or less transparent tissues. Using zebrafish blastula-stage embryos, which have a spherical geometry with the yolk and consequently form a thick tissue to image from the side, we tapped the trailing probe on the animal pole tissue, using fish medium and a later somitogenesis stage embryo as controls (Figures 7B-C, Movie S4). Shortly after probe contact with the animal pole the front

becomes obscured by the tissue and can no longer be tracked (Figure 7C, arrow) but the extended dye is clearly trackable. This allows an accurate determination of the animal pole blastoderm's response to the probe (Figures 7D-E), which suggests that it is softer than the dorsal tissue of the later stage embryo. These experiments show the feasibility of TiFM2.0 for side measurements of thicker tissues and a different model organism following probe modifications.

DISCUSSION

In this work we provided proof-of-concept demonstrations of the versatility of TiFM2.0 in probing and perturbing tissue mechanics in early vertebrate embryos. These experiments can reveal new biological insights, in combination with other mechanical tools, imaging and molecular approaches[11,30]. Notably, the collection of evidence so far starts to constitute a new level of understanding on the tissue mechanics of the avian embryonic posterior body. The tissues are produced at the posterior end and follow a posterior to anterior differentiation gradient that is now also revealed to be in parallel with a mechanical property gradient. The PSM cells, upon exiting the progenitor domain and entering the PSM, simultaneously drive tissue expansion and softening as they exhibit high motility and reorganize the ECM to absorb water[11,44,45]. This orients PSM deformation towards the posterior, and promotes the deformation of axial tissues such as the neural tube towards narrowing (including convergence and folding) and extension[9,29,54]. The stiffer axial tissues push through the "melting" progenitor domain (undergoing epithelial-mesenchymal transition[55]) containing new PSM cells, bisecting them to supply the bilateral sides[9]. These mechanical patterns and interactions enable directionality, tissue coupling and a robust speed[11], as well as potentially other key features of the body axis such as bilateral symmetry. TiFM here provides important direct measurements and controlled perturbations that put this description into proper physical context.

An important next step is to quantitatively interpret mechanical patterns and heterogeneities in the embryonic tissues uncovered by TiFM2.0. The *in situ* probing of tissue mechanics at the scale relevant for morphogenesis (~30-100μm) faces the challenge of an inhomogeneous and complex surrounding that in many cases can make the source of stress/resistance to the probes unclear, as early embryonic tissue sizes are comparable to the scale of measurement. Physically separating different tissues (such as by microsurgery) that could contribute to the probe dynamics would likely disrupt key ECM links between tissues and introduce mechanical effects at the wounds (such as tension increase), limiting the effectiveness of experimental dissection of different contributors. A potential solution will be to create a multi-tissue simulation framework where probe dynamics are predicted from a set of mechanical properties in different tissues and their links, which are fitted with experimental data at many locations across the embryo. This approach will establish a comprehensive picture on how tissue properties coordinate complex morphogenesis. The avian embryonic body axis here provides an excellent model for this type of systematic deconstruction of mechanical interactions. The understanding gained will illuminate human development during these stages when many defects arise, and where comparable processes have not been described due to the scarcity of embryo samples. More generally, the rationale and approaches of TiFM applied here to the body axis model are widely relevant to other classes of fundamental morphogenesis processes.

While TiFM2.0 as described in the current work contains a variety of modules and a complex user protocol, the core mechanism and function of TiFM systems as a controlled cantilever are simple, and can be deployed in a compact, easy-to-construct version (see methods – simple TiFM) or upgraded to work with high resolution microscopy, suited for large tissue-level measurement and perturbations or dynamic observation of cellular and molecular changes associated with tissue forces, respectively. Moreover, the system can be combined with other mechanical modules such as tension[50] and magnetic[27] controllers to enable multiplexed mechanical measurement and perturbation. Continued innovations in probe design and positioning as well as theoretical modelling for data quantification will further improve the applicability of TiFM systems and reduce their footprint and cost, enabling potentially wide use in developmental biology research and other settings.

Author Contributions: F.X. designed the project. A.R.H. developed the incubation module and protocol; Y.L. developed the trailing probe label and performed all zebrafish experiments; A.R.H., Y.L. and F.X. performed most calibration and chicken embryo experiments, and analysed the data; F.J. designed and created the double probe holder; F.J., S.B.P.M., J.M.N.V., Y.D., R.L., E.H., L.D.M. and L.B. contributed to conceptualization, experiments, protocols and analysis tools. A.R.H., Y.L. and F.X. prepared the manuscript. E.H. contributed to writing.

Acknowledgement: The authors thank C.U. Chan and members of the K. Kawaguchi lab for suggestions on the system design and data analysis; members of the Xiong lab for reagents, technical assistance, and comments; Chun Yuan Hii and Clare Buckley for assistance with zebrafish embryos, which were obtained through the fish facility at the Department of Physiology, Development and Neuroscience of University of Cambridge; Charles Bradshaw (Gurdon institute) and James Steele (the Maxwell Centre of University of Cambridge) for 3D printing; Michela Geri and Gareth McKinley for sharing the OWCh software and suggestions; Chiu Fan Lee for suggestion of the mechanical propagation experiment. This study is supported by a Wellcome Trust / Royal Society Sir Henry Dale Fellowship (215439/Z/19/Z) and a UKRI-EPSRC Frontier Research Grant (EP/X023761/1, originally selected as an ERC Starting Grant) to F.X. A.R.H. also acknowledges an SBS-Gurdon Studentship. Y.L. also acknowledges a Cambridge International Scholarship. F.J. and L.B. also acknowledges a Herschel Smith Postdoctoral Fellowship. F.J. also acknowledges a Wellcome Early Career Award (302541/Z/23/Z). Y.D. also acknowledges an LSI-Gurdon exchange programme supported by China Scholarship Council. R.L. also acknowledges a Xuetang summer scholarship from Tsinghua University. L.D.M. also acknowledges a Wellcome Trust PhD studentship (222274/Z/20/Z). The authors declare no competing interest.

MATERIALS & METHODS

List of hardware components. An equipment and component list is provided for the TiFM2.0 system. The table is organized by different modules. A simple/minimal TiFM setup is highlighted by selective components. It is not necessary to procure identical items. In particular, accessories such as connecting parts and scaffolds should be chosen according to the configuration of the base microscope. Basic instrument construction knowledge is needed to assemble the systems.

Module	Component	Function and notes	Source	Part# or link	Simple TiFM
Probe head	AFM chip and probes	Inserting into sample as a cantilever	Brukers, NanoWorld, BudgetSensors	MLCT-O10, ARROW-TL2, AIO-TL	x
	Electrical piezo	Controlling chip location in the x axis	Thorlabs	PB4NB2W	x
	Custom chip holder	Fitted with reflective mirrors	this study*		x
	Custom piezo holder		this study*		x
	Various connecting rods	Selected depending on the configuration	Thorlabs	https://www.thorlabs.com	x
	(master) Micromanipulator XYZ	Adjusting the overall location of probe 1 and 2 relative to the sample	World Precision Instruments	WPI M3301R	x
	(secondary) Micromanipulator YZ	Adjusting the location of probe 2 for alignment	Thorlabs	NF15AP25	
	Rails and support scan folds	Supporting the probehead construct and connecting to the base microscope	Thorlabs	https://www.thorlabs.com	x
	Wires and connectors	Connecting the piezo to the voltage controller	Rapid Electronics	https://www.rapidonline.com/	x
	Voltage controller	Sending driving programs to the electrical piezo, voltages are related to X_C although offsets and an error margin exist	Thorlabs	MDT693B	x
Base Microscope	Inverted widefield and fluorescence. Axio Observer 7, 2.5/5/10/20x objectives, XY motorized stage, side camera port, fluorescence filters and LED light source for RL imaging, objective holder Z-axis recording, associated controllers	Visualization of the probes (X_T) and the sample. Different magnifications are Essential for adjusting probe location followed by fine alignment. Z-axis recording is essential for determining probe insertion depth. Top illumination and condenser removed to allow installation of the probehead	Zeiss	https://www.micro-shop.zeiss.com/en/uk/system/inverted+microscopes-axio+observer-microscopes/6001/	x (any inverted scope)
	Goose neck top illumination	Providing side illumination and flexibly enhancing contrast of probe images	VWR	631-1086	
	Camera	Depending on applications needed, such as spatial temporal resolution, camera speed and sensitivity are chosen accordingly	Ximea	MQ042RG-CM	x (any camera)
Interferometer	Picoscale Interferometer and breakout box	Providing precision measurement of the location of the probe holder (X_C)	SmarAct	PS-CTRL-V2.0, PS-BOB-V2.0	
	Sensor head F01, F04	Working distance and angular tolerance need to be selected to balance the alignment requirement while keeping proper distance from sample and probe holders	SmarAct	PS-SH-F01, PS-SH-F04	
	Optical fibre cables		SmarAct	PS-ACC-PAT-APC-5M-APC-D	
	Scaffolds and rails	Selected depending on the configuration	Thorlabs	https://www.thorlabs.com	
	Micromanipulator XYZ	Adjusting interferometer sensor head in XYZ	Thorlabs	XR50P	
	Adjustable sensor holder	Adjusting interferometer sensor head's angle	Thorlabs	MK05	
	Trigger signal generator, Arduino linking camera and breakout box	Enabling synchronization of the camera (tip image, X_T) and the interferometer sensor (X_C) for real time stress dynamics	Rapid Electronics	75-0999	
Incubation	Programmable fluid pump	Providing a steady and slow water flow to maintain sample humidity	World Precision Instruments	AL-4000	
	Heating insert with sensors and feedback control	Maintaining stable temperature for the sample	Warner Instruments	TC-324C, DH-35	
	Fluid tubing and glass pipette	Guiding water to the required sample area	n/a		
System Computer	PC with >10 USB ports	Controlling all components and recording data	Dell	https://www.dell.com/	x

*Custom components include the motor and AFM chip holder module, and were printed by a 3D Printer (UltiMaker 3, Print Core AA 0.40) using PLA filament (2.85mm, RS PRO 832-0273). A tailored mirror (Silicon wafer, N-Phos) was glued to the outer side of the AFM chip holder for interferometer positioning. The engineering models and other details are available upon request.

Working environment and maintenance. TiFM systems should ideally be set up with vibration-isolation in quiet areas with stable temperature and humidity, and minimal dust. All wire connections should be checked regularly to ensure proper connection. The optical fibre wires should not be acutely bent or under tension. The piezo, probe holder and probes should be uninstalled from the probe head micromanipulators and stored in safe boxes when not in use as they are fragile. When installing the probe chips, a stand for the probe holder is recommended to free both hands. Under good lighting where the thin cantilever(s) is visible by naked eye, the user picks up the probe chip with a pair of sharp tweezers, holding the chip while staying away from the end with cantilevers, and insert the chip into the holder slot, before tightening with the screwdriver. When installing the probe holder to the scaffold and micromanipulators, take care to securely connect the piezo cables to the out cable from the voltage controller with the right match to avoid damaging the piezo. Upon finishing the experiments, use a clean imaging dish filled with deionized water to rinse the probe by dipping the chip/probe into the water a few times using the micromanipulator, before uninstalling the probe and holders.

Operation protocols. When ready to use the TiFM system, power up all hardware and open all controller software on the PC. In the following Ximea Cam tool (Ximea), MT voltage controller (Thorlabs), and Picoscale interferometer software (SmarAct) are used as examples to outline the protocol, which can be adapted to other hardware and software accordingly. First, check if the acquisition systems are functioning normally by starting live imaging, and change voltage input to move the piezo. Next, prepare an embryo sample and mount it on the imaging dish as desired for the actual measurements, add a few drops of PBS/Ringers solution on top to prevent drying (thin albumen is also ok with strong probes such as 0.2N/m but may damage the weaker ones due to its adhesion and viscosity). Mount the dish on the stage, position it so that the area of interest is centered, turn on the gooseneck LEDs to provide illumination. Use 2.5x, 5x and 10x objectives to observe the embryo with the camera, adjust the lighting angles and exposure times as necessary. Next, focus on the tissue of interest under 10x, record the focus positions of the tissue surface and the depth of interest, leaving the focus unchanged for probe adjustment. Remove the sample dish and lower the scaffold holding the piezo and chip/probe, carefully approach the stage to avoid collision with the objective and centre the probe tip at the pre-determined focal plane using the XYZ micromanipulator. This ensures the tip and the tissue of interest will be aligned. Use the second YZ micromanipulator to align the second probe to the desired relative position with the first probe, usually at the same focal plane / z-axis position, if applicable.

When the probes are in position, the interferometer sensor should be aligned to the probe holders. First algin the sensor head roughly with the holder mirror using the guide laser. Then in the Picoscale software, use the “Adjustment” mode to obtain the signal pattern on screen, while adjusting the position and angle of the sensor holder to improve the alignment as evaluated by the pattern score, using the

micromanipulators and the two angular controllers of the mirror mount. Leave the sensor holders untouched once a good signal is obtained (quality>60), continue with automatic adjustment and wait until the software indicates that the sensor channel is valid. Next set up the trigger signal required for the camera to activate the measurements to achieve synchronization following the software instructions. Open the data stream monitor and assign the trigger. Set up the camera to send the trigger signal upon activating frames (i.e., image acquisition). Test the trigger by starting live stream of the camera, the interferometer signal should immediately show on the monitor plot.

With probe and interferometer stand-by, the control sequence can be performed, followed by the samples. For the control run, image an empty or water sample with the moving probe under the same voltage program to be used on the embryo tissues, such as a step/ramp push for loading experiments, or an oscillatory movement for rheology experiments. Record the image set and interferometer readings. Before lifting the probe holder to allow mounting of the embryo sample, mark the position of the probe tip on the screen, as it will be difficult to see the probe tip directly before it making contacting the sample, once the sample is between the probe and the microscope. This mark helps when positioning the sample to the extract desired location of probe insertion. After mounting the embryo sample, adjust the focus to determine the location of the top surface of the sample, record the Z position of the surface and the probe tip Z position after insertion. These numbers help determine the insertion depth and probe-tissue contact area. This is not required for thin tissues, where the tissue thickness and probe width determine the contact area. To insert the probe into the sample, now without a clear visual of the probe tip, lower the probe holder in Z slowly and carefully while watching the changes on the live camera stream. The probe would change the lighting seen on the live stream and cast a shadow when it enters the tissue. Adjust the focus slightly to ensure a good contrast of the probe tip at the correct Z level of the tissue of interest. Depending on the experimental goals, a small ROI for the camera and memory-based high frame-rate acquisition mode may be desired for capturing fast probe dynamics. In those cases, adjust exposure time and lighting angles/intensity to maximize contrast at high frame-rate. Note that lower resolution, wider field of view images should also be taken to assess the range of tissue deformation. Collect the data obtained in a measurement run and record the corresponding measurement program for downstream analysis.

Control samples. A semi-dilute polymer solution of 8.5%w/w poly-isobutylene in hexadecane (PIB) (Sigma-Aldrich: 181455, H6703) was used. Hydrogel substrates were prepared following a protocol previously described[56,58], where the stiffness of the hydrogel solutions was directly measured using Atomic Force Microscopy (AFM). Briefly, 150µL of the solutions described in the table below were sandwiched between two glass coverslips and left to polymerize for 20min. The gels were hydrated in PBS for 30 minutes, after which one coverslip was carefully removed, exposing the hydrogel. The hydrogel was then immobilized on a plastic 35mm dish using vacuum grease, placed on the TiFM and measured.

Reagent	79Pa	369Pa	1100Pa	3130Pa	5220Pa	Source
40% Acrylamide [mL]	0.75	0.75	0.75	1	1.875	Bio-Rad 1610140
2% Bis-acrylamide [mL]	0.18	0.3	0.5	1.125	0.375	Bio-Rad 1610142
PBS [mL]	9.005	8.885	8.75	7.875	7.685	
To 1mL add:						
TEMED [µL]	15	15	1	1	15	Thermofisher 17919
10% Ammonium persulfate [µL]	50	50	10	10	50	Fisher Scientific 50-995-775

Chicken embryos. Wild type chicken (*Gallus gallus*) eggs were supplied Medeggs Inc. Tg(CAG-GFP)[57] and Tg(CAG-memGFP)[46] chicken eggs were provided by the National Avian Research Facility (NARF) at University of Edinburgh. Eggs were stored in 15°C fridge and incubated in 37.5°C ~60% humidity incubators (Brisnea) for 24 hours for the HH4 early-stage experiment, ~40 hours to reach HH stage 10-12 for the body axis experiments, and 72 hours for the blood pressure experiment. Embryos were prepared using a modified EC culture[59] protocol as described and incubated in a slide box lined with wet paper towels. Prior to TiFM experiments, embryos were further stabilized via a filter paper sandwich using enlarged windows to mitigate excess tension[50] and mounted on a glass bottom image dish with a thin layer of albumen or agarose-albumen culture media[29]. A small amount of PBS or Ringer's solution was added on top of the embryo prior to probe insertion for short-term experiments. For longer-term experiments, the water compensation pipette and pump were used at a flow rate of 8 µL/min, with a solution of 70% dH_2O, 20% Ringers, 10% thin albumen. When the heating insert is used, the outer ring temperature was set at 42°C to allow the dish centre to reach ~36°C at the embryo location.

Zebrafish embryos. Wild-type zebrafish AB and TL strains were used. Embryos were kept in 1X Embryo medium (E3 medium, reagents included: NaCl, KCl, $CaCl_2 \cdot H_2O$, $MgSO_4 \cdot 7H_2O$, HEPES, ddH_2O, pH to 7.4 with 10M NaOH) at 28.5°C. After dechorionation the embryos were kept in 1X E3 medium in a culture dish covered with agarose gel at 28.5°C. To hold the fish embryos and prevent rotations during measurements, a thin layer of 2% agarose was laid on the imaging dish, which was dug into with pipette tips to create two intersecting circles. E3 fish medium was then added to the imaging dish followed by loading the dechorionated embryo into one of the circles. The tissue to be tested is then rotated to face the opening between the 2 circles. The extra medium was then removed, leaving only a sufficient amount to cover the embryo. The probe was then inserted into the other circle, close to the test tissue. To ensure reliable tracking of the probe once it enters thicker tissue areas, a DiI-Epoxy bead was glued to the end of the cantilever to make a fluorescent trailing probe and imaged fluorescence.

Data analysis. Movies were analysed in Fiji (ImageJ). To track the probe(s), the raw movies were cropped into small sections containing the range of the probe movement. Linear adjustments (Brightness and contrast) were applied to sharpen the probe vs sample contrast. These processed movies were then used as input

together with the meta information file (time stamps) and the interferometer data output file in a custom analysis script, to obtain the tracks of the probe(s) and the holder positions for downstream analysis. To estimate forces on the probe, deflection was determined by comparing the tracks in the sample with tracks in the control (no-resistance) run, as described in the text.

References

1. Moon, L.D., and Xiong, F. (2021). Mechanics of neural tube morphogenesis. Semin Cell Dev Biol. https://doi.org/10.1016/J.SEMCDB.2021.09.009.
2. Mongera, A., Michaut, A., Guillot, C., Xiong, F., and Pourquié, O. (2019). Mechanics of anteroposterior axis formation in vertebrates. Annu Rev Cell Dev Biol *35*, 259–283. https://doi.org/10.1146/annurev-cellbio-100818-125436.
3. Guillot, C., and Lecuit, T. (2013). Mechanics of epithelial tissue homeostasis and morphogenesis. Preprint at American Association for the Advancement of Science, https://doi.org/10.1126/science.1235249 https://doi.org/10.1126/science.1235249.
4. Sutlive, J., Xiu, H., Chen, Y., Gou, K., Xiong, F., Guo, M., and Chen, Z. (2022). Generation, Transmission, and Regulation of Mechanical Forces in Embryonic Morphogenesis. Small *18*. https://doi.org/10.1002/SMLL.202103466.
5. Stooke-Vaughan, G.A., and Campàs, O. (2018). Physical control of tissue morphogenesis across scales. Curr Opin Genet Dev *51*, 111–119. https://doi.org/10.1016/j.gde.2018.09.002.
6. Adams, D.S., Keller, R., and Koehl, M.A.R. (1990). The mechanics of notochord elongation, straightening and stiffening in the embryo of Xenopus laevis. Development *110*, 115–130. https://doi.org/10.1111/j.0022-1112.2005.00688.x.
7. Chan, C.J., Costanzo, M., Ruiz-Herrero, T., Mönke, G., Petrie, R.J., Bergert, M., Diz-Muñoz, A., Mahadevan, L., and Hiiragi, T. (2019). Hydraulic control of mammalian embryo size and cell fate. Nature *571*, 112–116. https://doi.org/10.1038/S41586-019-1309-X.
8. Shyer, A.E., Huycke, T.R., Lee, C., Mahadevan, L., and Tabin, C.J. (2015). Bending gradients: how the intestinal stem cell gets its home. Cell *161*, 569–580. https://doi.org/10.1016/J.CELL.2015.03.041.
9. Xiong, F., Ma, W., Bénazéraf, B., Mahadevan, L., and Pourquié, O. (2020). Mechanical Coupling Coordinates the Co-elongation of Axial and Paraxial Tissues in Avian Embryos. Dev Cell *55*, 354-366.e5. https://doi.org/10.1016/j.devcel.2020.08.007.
10. Eritano, A.S., Bromley, C.L., Bolea Albero, A., Schütz, L., Wen, F.L., Takeda, M., Fukaya, T., Sami, M.M., Shibata, T., Lemke, S., et al. (2020). Tissue-Scale Mechanical Coupling Reduces Morphogenetic Noise to Ensure Precision during Epithelial Folding. Dev Cell *53*, 212-228.e12. https://doi.org/10.1016/j.devcel.2020.02.012.
11. Lu, C., Vidigueira, J.M.N., Jie, C.C.J., Maksymiuk, A., and Xiong, F. (2024). Cell density couples tissue mechanics to control the elongation speed of the body axis. iScience *27*, 110968. https://doi.org/10.1016/J.ISCI.2024.110968.
12. van den Brink, S.C., Alemany, A., van Batenburg, V., Moris, N., Blotenburg, M., Vivié, J., Baillie-Johnson, P., Nichols, J., Sonnen, K.F., Martinez Arias, A., et al. (2020). Single-cell and spatial transcriptomics reveal somitogenesis in gastruloids. Nature *582*, 405. https://doi.org/10.1038/s41586-020-2024-3.
13. Xiong, F., and Megason, S.G. (2015). Abstracting the principles of development using imaging and modeling. Integrative Biology *7*, 633–642. https://doi.org/10.1039/c5ib00025d.
14. Campàs, O. (2016). A toolbox to explore the mechanics of living embryonic tissues. Preprint at Academic Press, https://doi.org/10.1016/j.semcdb.2016.03.011 https://doi.org/10.1016/j.semcdb.2016.03.011.
15. Chanet, S., Miller, C.J., Vaishnav, E.D., Ermentrout, B., Davidson, L.A., and Martin, A.C. (2017). Actomyosin meshwork mechanosensing enables tissue shape to orient cell force. Nat Commun *8*. https://doi.org/10.1038/ncomms15014.
16. Bertet, C., Sulak, L., and Lecuit, T. (2004). Myosin-dependent junction remodelling controls planar cell intercalation and axis elongation. Nature *429*, 667–671. https://doi.org/10.1038/nature02590.
17. Riedl, J., Crevenna, A.H., Kessenbrock, K., Yu, J.H., Neukirchen, D., Bista, M., Bradke, F., Jenne, D., Holak, T.A., Werb, Z., et al. (2008). Lifeact: a versatile marker to visualize F-actin. Nat Methods *5*, 605–607. https://doi.org/10.1038/NMETH.1220.

18. Xiong, F., Ma, W., Hiscock, T.W., Mosaliganti, K.R., Tentner, A.R., Brakke, K.A., Rannou, N., Gelas, A., Souhait, L., Swinburne, I.A., et al. (2014). Interplay of cell shape and division orientation promotes robust morphogenesis of developing epithelia. Cell *159*, 415–427. https://doi.org/10.1016/j.cell.2014.09.007.
19. Merkel, M., and Manning, M.L. (2017). Using cell deformation and motion to predict forces and collective behavior in morphogenesis. Semin Cell Dev Biol *67*, 161–169. https://doi.org/10.1016/j.semcdb.2016.07.029.
20. Campinho, P., Behrndt, M., Ranft, J., Risler, T., Minc, N., and Heisenberg, C.P. (2013). Tension-oriented cell divisions limit anisotropic tissue tension in epithelial spreading during zebrafish epiboly. Nature Cell Biology 2013 15:12 *15*, 1405–1414. https://doi.org/10.1038/ncb2869.
21. Sampayo, R.G., Sakamoto, M., Wang, M., Kumar, S., and Schaffer, D. V. (2023). Mechanosensitive stem cell fate choice is instructed by dynamic fluctuations in activation of Rho GTPases. Proc Natl Acad Sci U S A *120*. https://doi.org/10.1073/PNAS.2219854120.
22. Yamamoto, K., Miura, H., Ishida, M., Mii, Y., Kinoshita, N., Takada, S., Ueno, N., Sawai, S., Kondo, Y., and Aoki, K. (2021). Optogenetic relaxation of actomyosin contractility uncovers mechanistic roles of cortical tension during cytokinesis. Nat Commun *12*. https://doi.org/10.1038/S41467-021-27458-3.
23. Prevedel, R., Diz-Muñoz, A., Ruocco, G., and Antonacci, G. (2019). Brillouin microscopy: an emerging tool for mechanobiology. Nature Methods 2019 16:10 *16*, 969–977. https://doi.org/10.1038/s41592-019-0543-3.
24. Mulligan, J.A., Untracht, G.R., Chandrasekaran, S.N., Brown, C.N., and Adie, S.G. (2016). Emerging Approaches for High-Resolution Imaging of Tissue Biomechanics With Optical Coherence Elastography. IEEE Journal of Selected Topics in Quantum Electronics *22*, 246–265. https://doi.org/10.1109/JSTQE.2015.2481705.
25. Dal Molin, M., Verolet, Q., Colom, A., Letrun, R., Derivery, E., Gonzalez-Gaitan, M., Vauthey, E., Roux, A., Sakai, N., and Matile, S. (2015). Fluorescent flippers for mechanosensitive membrane probes. J Am Chem Soc *137*, 568–571. https://doi.org/10.1021/JA5107018/SUPPL_FILE/JA5107018_SI_001.PDF.
26. C, R., CJ, C., B, G., T, H., and F, G. (2021). Inferring cell junction tension and pressure from cell geometry. Development *148*. https://doi.org/10.1242/DEV.192773.
27. Serwane, F., Mongera, A., Rowghanian, P., Kealhofer, D.A., Lucio, A.A., Hockenbery, Z.M., and Campàs, O. (2017). In vivo quantification of spatially varying mechanical properties in developing tissues. Nat Methods *14*, 181–186. https://doi.org/10.1038/nmeth.4101.
28. Campàs, O., Mammoto, T., Hasso, S., Sperling, R.A., O'connell, D., Bischof, A.G., Maas, R., Weitz, D.A., Mahadevan, L., and Ingber, D.E. (2014). Quantifying cell-generated mechanical forces within living embryonic tissues. Nat Methods *11*, 183–189. https://doi.org/10.1038/nmeth.2761.
29. Chan, C.U., Xiong, F., Michaut, A., Vidigueira, J.M.N., Pourquié3pourquié3, O., and Mahadevan, L. (2023). Direct force measurement and loading on developing tissues in intact avian embryos. Development *150*. https://doi.org/10.1242/DEV.201054.
30. McLaren, S.B.P., Xue, S.-L., Ding, S., Winkel, A., Baldwin, O., Dwarakacherla, S., Franze, K., Hannezo, E., and Xiong, F. (2024). Differential tissue deformability underlies shape divergence of the embryonic brain and spinal cord under fluid pressure. bioRxiv, 2024.01.12.575349. https://doi.org/10.1101/2024.01.12.575349.
31. Dzementsei, A., Barooji, Y.F., Ober, E.A., and Oddershede, L.B. (2022). Foregut organ progenitors and their niche display distinct viscoelastic properties in vivo during early morphogenesis stages. Commun Biol *5*. https://doi.org/10.1038/S42003-022-03349-1.
32. Kato, S., and Inomata, H. (2023). Blastopore gating mechanism to regulate extracellular fluid excretion. iScience *26*. https://doi.org/10.1016/j.isci.2023.106585.
33. Wang, W., Pan, Y., Shui, Y., Hasan, T., Lei, I.M., Ka, S.G.S., Savin, T., Velasco-Bosom, S., Cao, Y., McLaren, S.B.P., et al. (2024). Imperceptible augmentation of living systems with organic bioelectronic fibres. Nature Electronics 2024, 1–12. https://doi.org/10.1038/s41928-024-01174-4.
34. Ghosh, A., Dasgupta, D., Pal, M., Morozov, K.I., Leshansky, A.M., Ghosh, A., Ghosh, A., Dasgupta, D., Pal, M., Morozov, K.I., et al. (2018). Helical Nanomachines as Mobile Viscometers. Adv Funct Mater *28*, 1705687. https://doi.org/10.1002/ADFM.201705687.
35. Lee, J.O., Park, H., Du, J., Balakrishna, A., Chen, O., Sretavan, D., and Choo, H. (2017). A microscale optical implant for continuous in vivo monitoring of intraocular pressure. Microsyst Nanoeng *3*, 1–9. https://doi.org/10.1038/micronano.2017.57.

36. McLaren, S.B.P., and Xiong, F. (2024). Lumen Pressure Modulation in Chicken Embryos. Methods in Molecular Biology - Tissue Morphogenesis *2805*, 161–169. https://doi.org/10.1007/978-1-0716-3854-5_11.
37. Dunsby, C. (2008). Optically sectioned imaging by oblique plane microscopy. Optics Express, Vol. 16, Issue 25, pp. 20306-20316 *16*, 20306–20316. https://doi.org/10.1364/OE.16.020306.
38. Sirinakis, G., Sirinakis, G., Allgeyer, E.S., Nashchekin, D., Johnston, D. St., and Johnston, D. St. (2024). User-friendly oblique plane microscopy on a fully functional commercially available microscope base. Biomedical Optics Express, Vol. 15, Issue 4, pp. 2358-2376 *15*, 2358–2376. https://doi.org/10.1364/BOE.518856.
39. Agero, U., Glazier, J.A., and Hosek, M. (2010). Bulk elastic properties of chicken embryos during somitogenesis. Biomed Eng Online *9*, 1–16. https://doi.org/10.1186/1475-925X-9-19/TABLES/3.
40. Delfini, M.C., Dubrulle, J., Malapert, P., Chal, J., and Pourquié, O. (2005). Control of the segmentation process by graded MAPK/ERK activation in the chick embryo. Proc Natl Acad Sci U S A *102*, 11343–11348. https://doi.org/10.1073/PNAS.0502933102/SUPPL_FILE/02933MOVIE4.MOV.
41. Chal, J., Guillot, C., and Pourquié, O. (2017). PAPC couples the segmentation clock to somite morphogenesis by regulating N-cadherin-dependent adhesion. Development (Cambridge) *144*, 664–676. https://doi.org/10.1242/dev.143974.
42. Bénazéraf, B., Beaupeux, M., Tchernookov, M., Wallingford, A., Salisbury, T., Shirtz, A.A., Shirtz, A.A., Huss, D., Pourquié, O., François, P., et al. (2017). Multi-scale quantification of tissue behavior during amniote embryo axis elongation. Development (Cambridge) *144*, 4462–4472. https://doi.org/10.1242/dev.150557.
43. Rifes, P., and Thorsteinsdóttir, S. (2012). Extracellular matrix assembly and 3D organization during paraxial mesoderm development in the chick embryo. Dev Biol *368*, 370–381. https://doi.org/10.1016/j.ydbio.2012.06.003.
44. Bénazéraf, B., Francois, P., Baker, R.E., Denans, N., Little, C.D., and Pourquié, O. (2010). A random cell motility gradient downstream of FGF controls elongation of an amniote embryo. Nature *466*, 248–252. https://doi.org/10.1038/nature09151.
45. Michaut, A., Mongera, A., Gupta, A., Serra, M., Rigoni, P., Lee, J.G., Duarte, F., Hall, A.R., Mahadevan, L., Guevorkian, K., et al. (2022). Activity-driven extracellular volume expansion drives vertebrate axis elongation. bioRxiv, 2022.06.27.497799. https://doi.org/10.1101/2022.06.27.497799.
46. Rozbicki, E., Chuai, M., Karjalainen, A.I., Song, F., Sang, H.M., Martin, R., Knölker, H.J., Macdonald, M.P., and Weijer, C.J. (2015). Myosin-II-mediated cell shape changes and cell intercalation contribute to primitive streak formation. Nat Cell Biol *17*, 397–408. https://doi.org/10.1038/ncb3138.
47. Nishimura, T., Honda, H., and Takeichi, M. (2012). Planar cell polarity links axes of spatial dynamics in neural-tube closure. Cell *149*, 1084–1097. https://doi.org/10.1016/j.cell.2012.04.021.
48. Roellig, D., Theis, S., Proag, A., Allio, G., Bénazéraf, B., Gros, J., and Suzanne, M. (2022). Force-generating apoptotic cells orchestrate avian neural tube bending. Dev Cell *57*, 707-718.e6. https://doi.org/10.1016/J.DEVCEL.2022.02.020.
49. Alvarez, I.S., and Schoenwolf, G.C. (1992). Expansion of surface epithelium provides the major extrinsic force for bending of the neural plate. Journal of Experimental Zoology *261*, 340–348. https://doi.org/10.1002/jez.1402610313.
50. Kunz, D., Wang, A., Chan, C.U., Pritchard, R.H., Wang, W., Gallo, F., Bradshaw, C.R., Terenzani, E., Müller, K.H., Huang, Y.Y.S., et al. (2023). Downregulation of extraembryonic tension controls body axis formation in avian embryos. Nature Communications 2023 14:1 *14*, 1–15. https://doi.org/10.1038/s41467-023-38988-3.
51. Maniou, E., Todros, S., Urciuolo, A., Moulding, D.A., Magnussen, M., Ampartzidis, I., Brandolino, L., Bellet, P., Giomo, M., Pavan, P.G., et al. (2024). Quantifying mechanical forces during vertebrate morphogenesis. Nature Materials 2024, 1–7. https://doi.org/10.1038/s41563-024-01942-9.
52. Marrese, M., Antonovaite, N., Nelemans, B.K.A., Smit, T.H., and Iannuzzi, D. (2019). Micro-indentation and optical coherence tomography for the mechanical characterization of embryos: Experimental setup and measurements on chicken embryos. Acta Biomater *97*, 524–534. https://doi.org/10.1016/j.actbio.2019.07.056.
53. Mongera, A., Rowghanian, P., Gustafson, H.J., Shelton, E., Kealhofer, D.A., Carn, E.K., Serwane, F., Lucio, A.A., Giammona, J., and Campàs, O. (2018). A fluid-to-solid jamming

transition underlies vertebrate body axis elongation. Nature *561*, 401–405. https://doi.org/10.1038/s41586-018-0479-2.
54. Regev, I., Guevorkian, K., Gupta, A., Pourquié, O., and Mahadevan, L. (2022). Rectified random cell motility as a mechanism for embryo elongation. Development (Cambridge) *149*. https://doi.org/10.1242/DEV.199423/VIDEO-2.
55. Goto, H., Kimmey, S.C., Row, R.H., Matus, D.Q., and Martin, B.L. (2017). FGF and canonical Wnt signaling cooperate to induce paraxial mesoderm from tailbud neuromesodermal progenitors through regulation of a two-step epithelial to mesenchymal transition. Development (Cambridge) *144*, 1412–1421. https://doi.org/10.1242/dev.143578.
56. Tse, J.R., and Engler, A.J. (2010). Preparation of Hydrogel Substrates with Tunable Mechanical Properties. Curr Protoc Cell Biol *47*, 10.16.1-10.16.16. https://doi.org/10.1002/0471143030.CB1016S47.
57. McGrew, M.J., Sherman, A., Lillico, S.G., Ellard, F.M., Radcliffe, P.A., Gilhooley, H.J., Mitrophanous, K.A., Cambray, N., Wilson, V., and Sang, H. (2008). Localised axial progenitor cell populations in the avian tail bud are not committed to a posterior Hox identity. Development *135*, 2289–2299. https://doi.org/10.1242/dev.022020.
58. Xi, W., Saleh, J., Yamada, A., Tomba, C., Mercier, B., Janel, S., Dang, T., Soleilhac, M., Djemat, A., Wu, H., et al. (2022). Modulation of designer biomimetic matrices for optimized differentiated intestinal epithelial cultures. Biomaterials *282*, 121380. https://doi.org/10.1016/J.BIOMATERIALS.2022.121380.
59. Chapman, S.C., Collignon, J.J., Schoenwolf, G.C., and Lumsden, A. (2001). Improved method for chick whole-embryo culture using a filter paper carrier. Developmental Dynamics *220*, 284–289. https://doi.org/10.1002/1097-0177(20010301)220:3<284::AID-DVDY1102>3.0.CO;2-5.

Figures

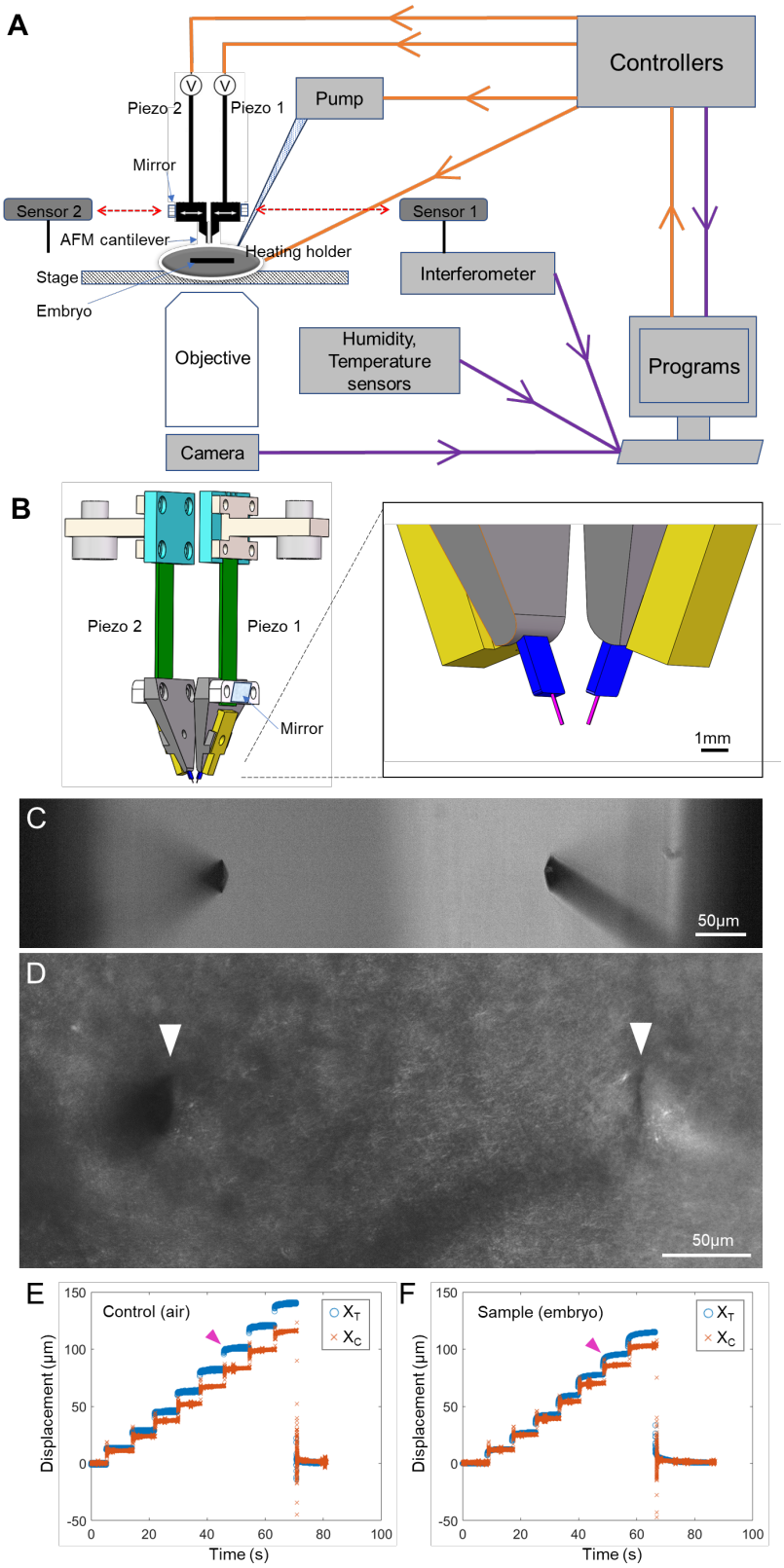

Figure 1. TiFM2.0 design
(A) Schematic of TiFM2.0 highlighting the design logic and main components.

(B) Drawing of the double motor probe holder. The blue probe chip and the pink cantilever probes are drawn in exaggerated sizes for illustration purpose.
(C) Example of double probes aligned in Z, microscope view in air (no samples).
(D) Example of double probes inserted in an embryonic tissue (HH4 epiblast).
(E) Example of a force loading control run in air. The holder was driven to make stepwise movements detected by the interferometer (x_C), the images provide tracking of the probe tip (x_T). In this no-resistance scenario, a difference between two tracks arises as the positions of the mirror and the probe tip are different in the Z axis and the piezo motor's X axis movement is achieved by bending. Arrowheads compare the probe movement dynamics after a step movement of the holder.
(F) Example of a force loading experimental run in an embryo (~HH11, medial-to-lateral loading on the body axis), following the control in panel E. Reduced probe movement at each step and creep (arrowhead) compared to the trace in panel E indicate sample resistance.

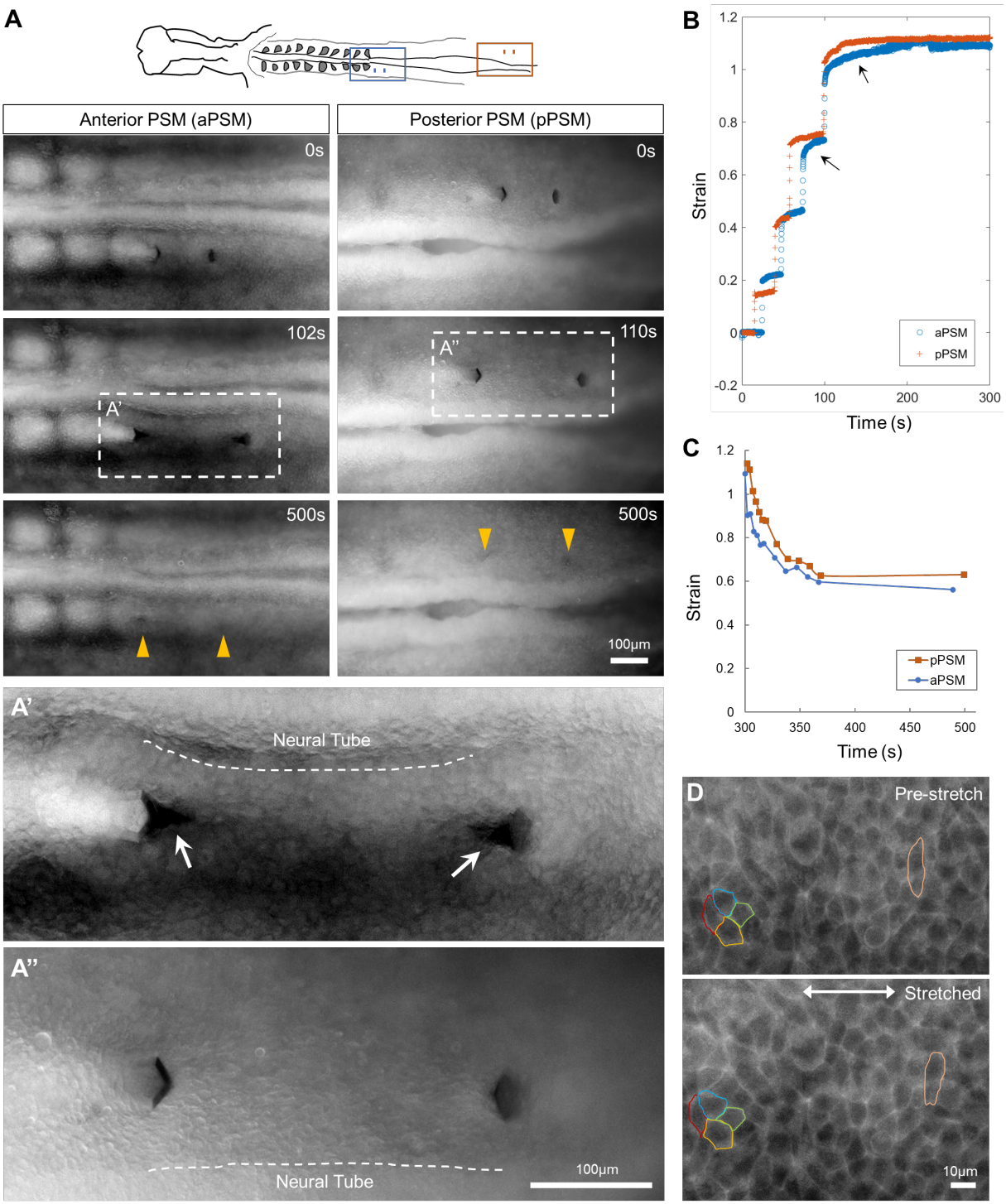

Figure 2. Local double probe stretching and tissue responses
(A) Stepwise stretching along the AP axis with 2 probes (Representative of N=5 different embryos). The schematic marks the locations in the embryo tested. Dashed line boxes correspond to zoomed-in views in panels A' and A''. Yellow arrowheads track the probe wounds. Dashed lines in A' and A'' mark the lateral side of the neural tube. Arrows in A' indicate the tissue tears.
(B) Strain dynamics following stepwise stretching. Tracked from the data in panel A. The tissue length between 2 probes at each step is compared with the original length. Arrows highlight the different creep rates between aPSM and pPSM.

(C) Strain dynamics following probe retraction. The timelapse movies continue from panel B. The probe wounds were tracked manually and the tissue length between 2 probes is compared with the original length.
(D) Cell shape changes under tension. HH4 mem-GFP+ anterior neural plate area was imaged through bidirectional stretching. The tracked cells are located near the middle of two probes. Contours were drawn following cell membrane outlines to show cell shape and cell junction changes. See also Movie S1.

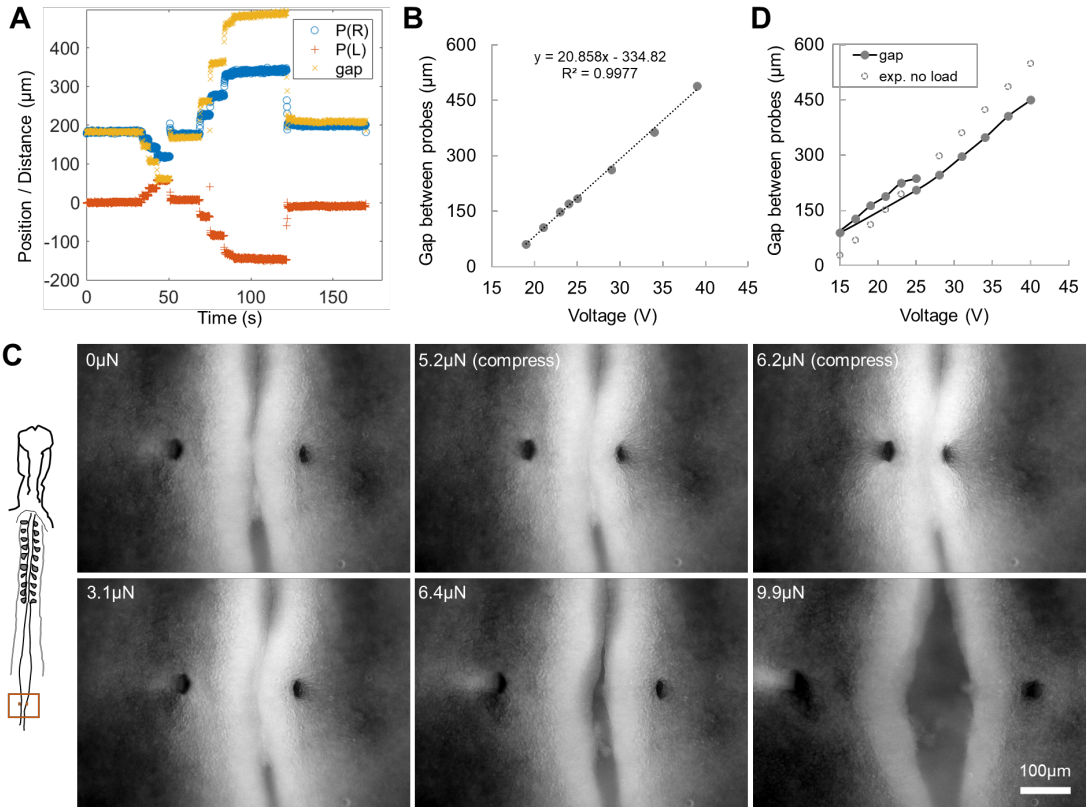

Figure 3. Compression and pulling of the neural folds
(A) Double probe tracks from a control timelapse movie.
(B) Calibration of probe gaps with the driving program.
(C) Images of the compressed and pulled neural folds under the driving program. Representative sample from N=4 embryos. The parallel bright tissues in the middle are the two neural folds. Forces labelled (in µN) represent force exerted on the probes (k = 0.2 N/m) by the neural folds during compression and pulling.
(D) Probe gaps over the course of the perturbation. Black line links the steps, starting from 25V. A roughly linear resistance increase is seen in both folding and unfolding directions.

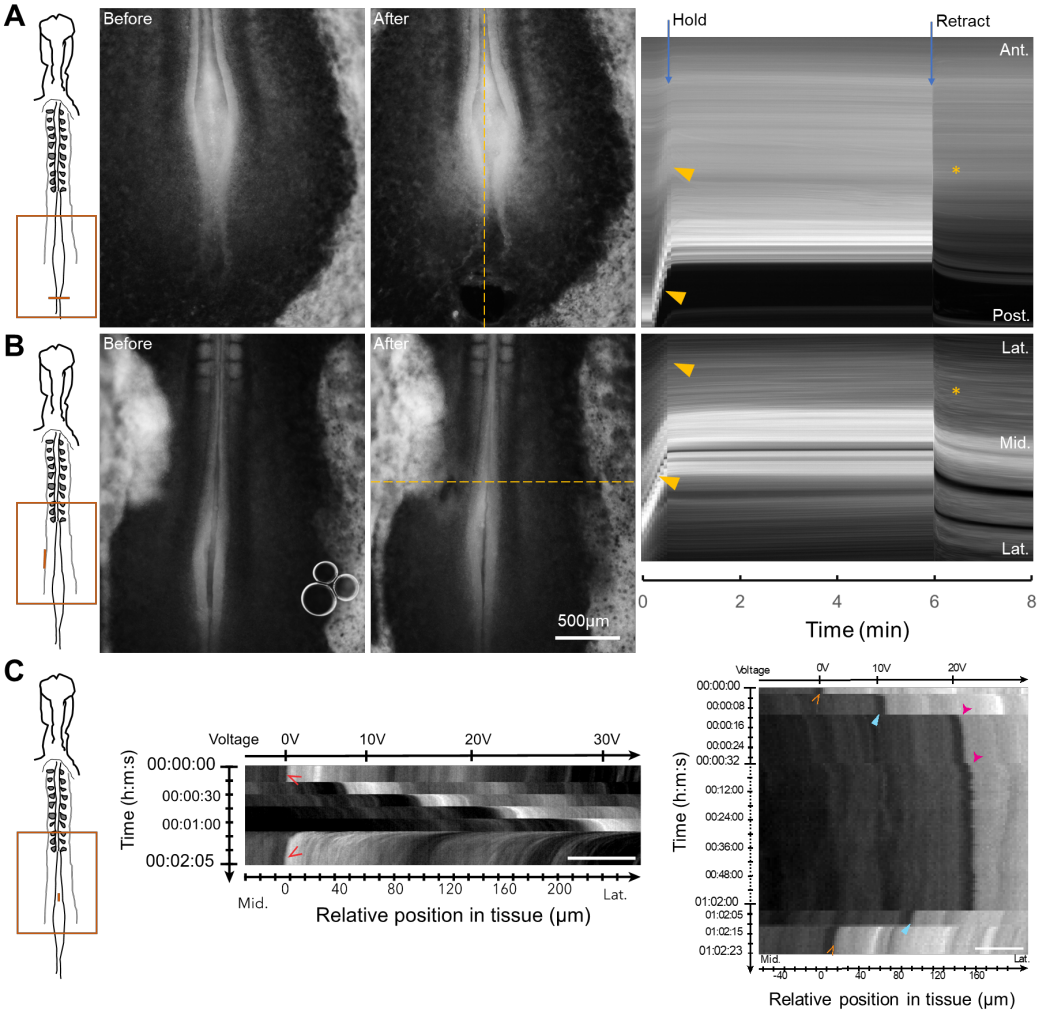

Figure 4. Mechanical anisotropy of AP and ML axes
(A, B) Posterior body axis anteroposterior (A) and mediolateral (B) compression using an aluminium foil probe (~400 µm wide). The probe was inserted just posterior to the neural tube and moved in the anterior direction ~600 µm (A) or inserted at the PSM-LPM border and moved ~400 µm towards the midline (B). Images taken immediately before and after compression are shown on the left. The yellow lines indicate the axes used for kymograph plotting (shown on the right). The kymograph is labelled with the points at which the maximum compression was achieved (Hold) and when the probe was retracted (Retract), ~5 min 30 sec later. Arrowheads in each image compare the extent of deformation under the probe at different distances from the probe where (A) shows more drop of slope between bottom and top arrowheads compared to (B). Asterisks compare the extent of recoil.
(C). Mediolateral compression using notochord anchored probe (~50 µm wide). Compression occurs for 1 minute: stepwise increment of voltage to a maximum of 30V and then immediate removal of load. Red arrows mark the initial and final position of the probe; the difference is 0µm (±2 µm). Compression held for 1hr: stepwise loading to a maximum of 20V, and subsequent release. Orange arrows mark the initial and final position of the probe, the final difference is 12µm (±2 µm). Blue arrows mark the position at 10V when loading and retracting, difference is 27µm (±2 µm). Magenta arrows mark the initial position of the probe at 20V and the position after ~5min of incubation, difference is 10µm (±2 µm). During incubation, images taken at 1min interval. Scale bars = 50µm.

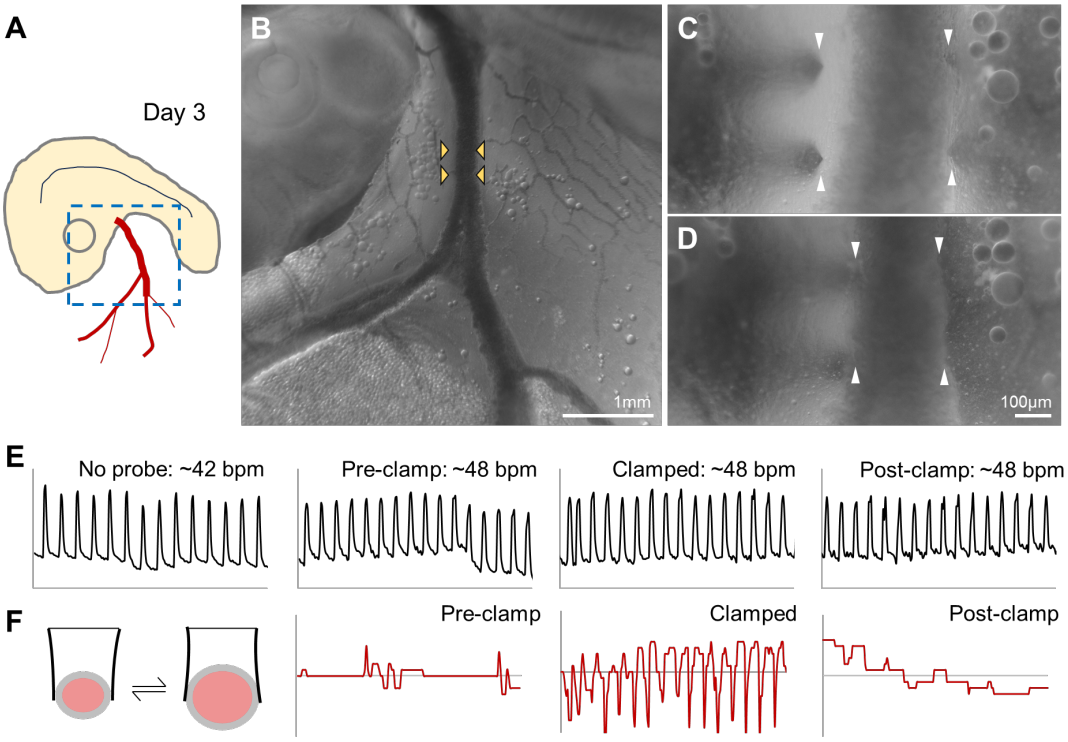

Figure 5. Blood pressure in the embryonic artery
(A) Diagram of a Day-3 embryo showing the imaged region and the right omphalomesenteric artery leading off the body.
(B) Zoomed out image of the region and the artery. Yellow arrowheads mark the insertion points of the double-pronged probes on both sides of the artery.
(C) Probes pre-clamp. The right-side probes are in contact with the artery wall.
(D) Probes clamping the artery after the left-side probes are moved to engage.
(E) Monitored heart rate of the embryo through the experiment.
(F) Diagram and measurement of probe movement. Heartbeats send a surge of blood flow through the artery and expand the vessel, generating a transient pressure on the probes.

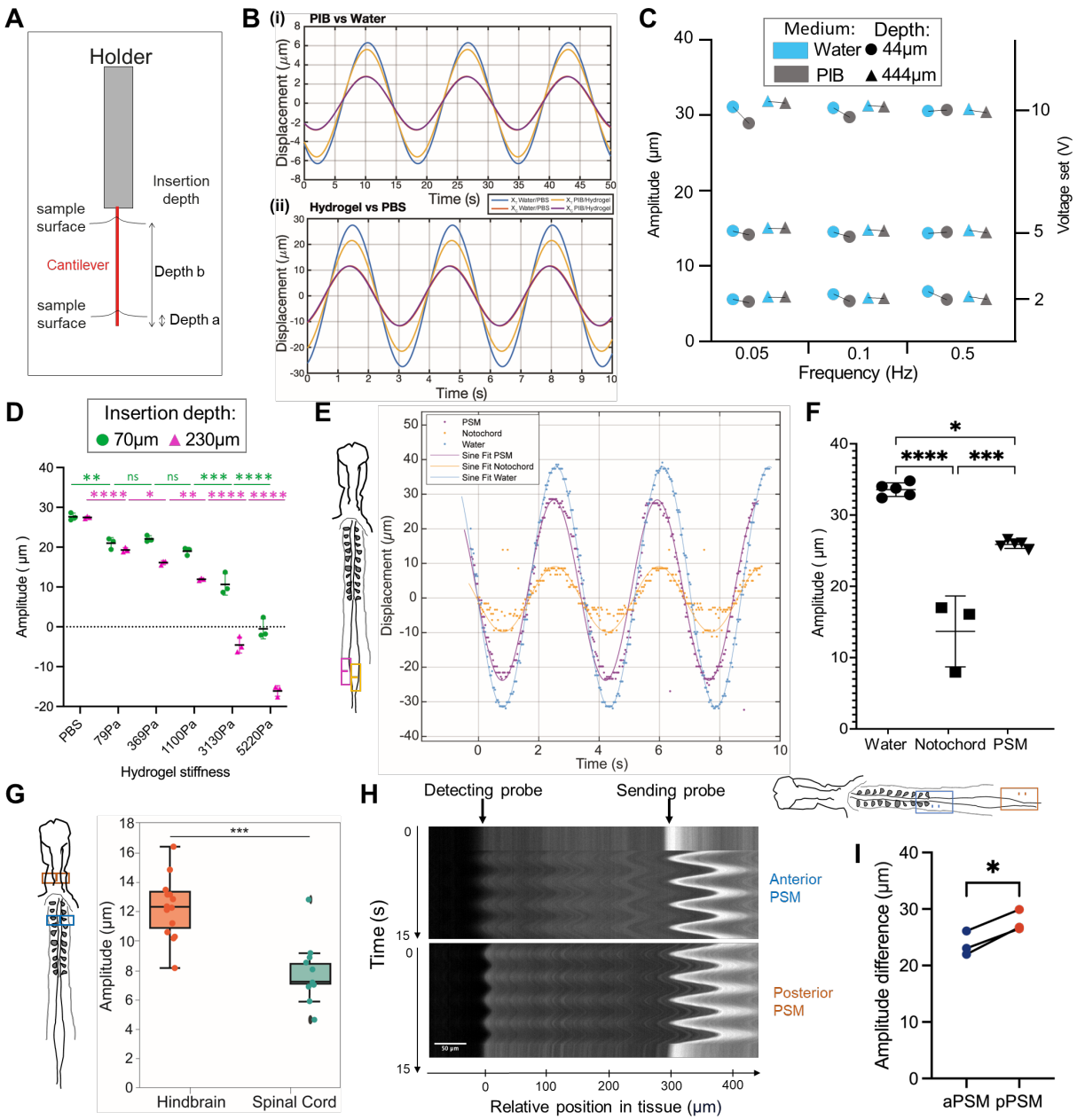

Figure 6. Tissue mechanical evaluation with oscillatory probe movements
(A) Diagram of single-probe mechanical tests at different depths and for different samples in panels B-G.
(B) Example comparison using the same driving program in water and PIB (**i**, 2V max, 0.1Hz sine wave, k = 0.31N/m) and in PBS and 369Pa Hydrogel (**ii**, 10V max, 0.5Hz sine wave, k = 0.2 N/m), respectively. The curves plotted were fitted sine waves on the raw data traces, then the interferometer traces of two samples were overlaid to highlight the subtle differences in amplitude and phase between the probe tip tracks.
(C) Comparison of probe amplitude between water and PIB. Comparison between 3 different voltages (2V, 5V and 10V), over 3 different sinusoid frequencies (0.05Hz, 0.1Hz and 0.5Hz), at two different depths (circle: 44 μm and triangle: 444 μm). Amplitude calculated by fitting between 2 and 7 full periods of the sin wave. Probe force constant k = 0.31N/m.

(D) Comparison of probe amplitude between PBS and hydrogels of varying stiffness. Probe force constant *k* = 0.2N/m, set to 10V and with a sinewave frequency of 0.5Hz, at two different insertion depths (circle: 70 µm and triangle: 230 µm). Negative amplitude is defined as tip movement in the opposite direction of the driving motor. Black line marks mean, error bars are ±SD. Turkey's multiple comparison test (n=3). At 70 µm: n.s 79Pa vs 369Pa p = 0.9685, n.s 369Pa vs 1100Pa p = 0.3101, ** p=0.0051, *** p=0.0008, **** p<0.0001. At 230 µm: * p=0.0258, ** p=0.0037, **** p<0.0001.
(E) Representative example of probe tip position tracking (marked by dots) and sin fitting (marked by line) across Water, PSM and notochord measurements. Sine fitting over n=2.5 periods.
(F) Amplitude differences between Water (n=5), Notochord (n=3) and PSM (n=5). Probe force constant *k* = 0.2N/m, at 10V, sinewave frequency of 0.5Hz. Tissue insertion depth is approximately 70µm. Turkey's multiple comparison test: * p=0.0152, *** p=0.0007, **** p=< 0.0001.
(G) Amplitude of probe (*k* = 0.02N/m) movement driven at 0.2Hz and 5V in the hindbrain (n=14) and spinal cord (n=10) of HH11-12 chicken embryos. Mann-Whitney U test, *** p<0.001.
(H) Kymographs representing double probe movement tracks for anterior (aPSM) and posterior (pPSM) locations. Representative of N=3 samples. Sending and detecting probe amplitude tracked by high contrast lines. Scale bar = 50µm.
(I) Amplitude difference between sending and detecting probes in anterior PSM (aPSM) and posterior PSM (pPSM). A smaller amplitude difference shows the detecting probe oscillates more in response to the sending probe, suggesting the tissue is stiffer. A large amplitude difference indicates the detecting probe does not respond to the imposed oscillation from the sending probe, suggesting a softer tissue. Paired t-test *p=0.0176, n=3.

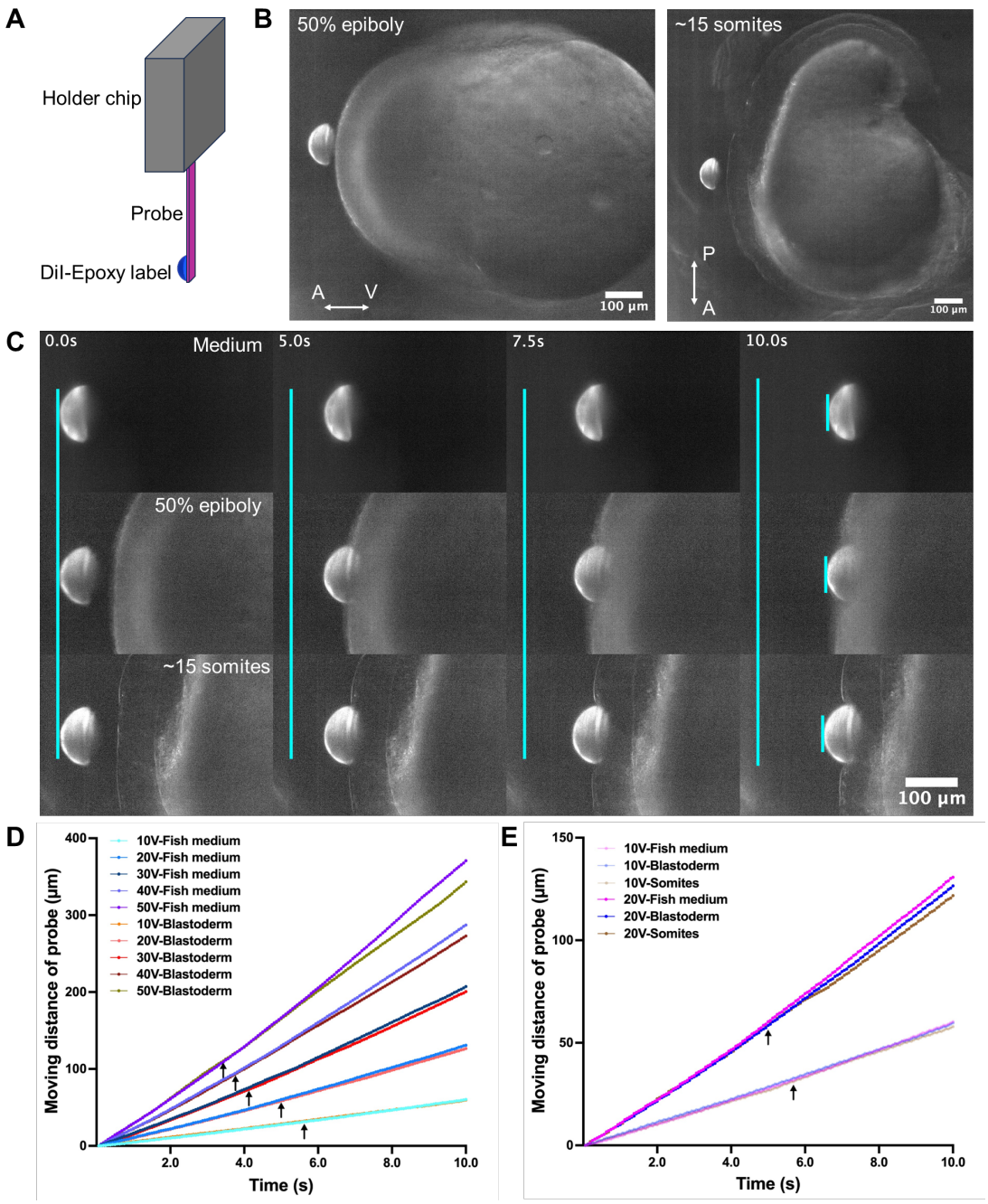

Figure 7. Tracking modified probe in thick tissues in zebrafish embryos
(A) Diagram of the probe with a DiI-Epoxy label.
(B) Example images of the labelled probe and the sample embryo. The animal pole at 50% epiboly (left) and the dorsal trunk during somitogenesis (right). Movies are taken with red fluorescence and a low level of background light to visualize the embryo tissues. A-V axis indicates animal-vegetal; P-A axis indicates posterior-anterior.
(C) Imaging of the probe movement when pushing different tissues under the voltage loaded on the probe of 20V, 0.1 Hz and Ramp function (linear movement of the motor). Fish medium (1st row), animal pole at 50% epiboly (2nd row) and dorsal trunk at ~15 somite stage (3rd row) are shown here as representative examples. Images show the probe position at the beginning of loading the voltage (1st column), starting to touch the tissue edges (2nd column), continuing to push the tissues (3rd

column) and the final position when the maximum voltage is reached (4th column). See also Movie S4.
(D) Resistance comparison (shown by maximum moving distance of the probe, tracked by the bright edge kymograph of the backend of the probe, same in panel E) of fish medium and animal pole at 50% epiboly from 10V to 50V maximum displacements.
(E) Resistance comparison of fish medium, animal pole at 50% epiboly and dorsal trunk at ~15 somite stage from 10V to 20V maximum displacements.

Movies

Movie S1. Cell shape changes under tension. HH4 mem-GFP+ anterior neural plate area was imaged through bidirectional stretching. Probe force constant k = 0.2N/m. Voltage controlling the double-motor was increased by 5V steps (to prevent tissue tearing) to eventually 40V and held for 1 hour. Timestamp shows minutes and seconds (imaging frequency was 2Hz). The movie shows the first 4 minutes of the experiment (a focus adjustment around 03:45). Probes can be seen exiting the field of view on the sides as the stepwise stretching continued. Tissue and cells can be seen to change shape in response to the imposed tension. Scale bar: 100μm.

Movie S2. Representative examples of raw imaging data of the probe tip in hydrogel samples. Probe force constant k = 0.2N/m, set to 10V and with a sinewave frequency of 0.5Hz, at an insertion depth of 230 μm. While the motor and probe holder move the same way in each sample, the probe movement can be seen to decrease as the stiffness increases. In very stiff samples, the probe is locally "stuck" and rotates around the half insertion point, resulting in the probe tip moving in an opposite direction to the motor (e.g., 3130Pa and 5220Pa).

Movie S3. Representative examples of raw imaging data of the probe tip in embryonic tissues. Probe force constant k = 0.2N/m, at 10V, sinewave frequency of 0.5Hz. Tissue insertion depth is approximately 70μm. While the motor and probe holder move the same way in each sample, the probe movement amplitudes are distinct. PSM, presomitic mesoderm.

Movie S4. Labelled probe pushing different tissues in zebrafish embryos. The probe moves linearly towards a maximum distance driven by the motor (20V, 0.1 Hz). Fish medium (1st row), animal pole at 50% epiboly (2nd row) and dorsal trunk at ~15 somite stage (3rd row). Probe front is obscured by tissue after contact and cannot be further tracked. Tracking the trailing dye bead allows comparison of tissue resistance.